Transition to Atomic Wire Electrode Actuates Gold-thiol Spin Valve

A. Prakash[1]
Department of Mechanical Engineering, University of Illinois, Urbana, Illinois

(Dated: January 4, 2021)

In resemblance of the mechanically-controlled break junction, we considered 1,4-benzenedithiol making ohmic contacts with gold in three distinct configurations of the gold electrodes. Simulations of non-equilibrium charge transport within density-functional theory, despite the time-frozen ansatz and the neglection of e-ph scattering, indicate that the transmission coefficient depends upon the spin state of the itinerant electron if the electrode is an atomic wire. The projected density of states at the Au-S interface for each Au-BDT junction determined that significant anisotropy of the spin-orbital occupations at the Fermi level occurs only for the atomic wire electrode. Current-voltage results indicate that the spin filtration ratio $(I_{\downarrow}/I_{\uparrow})(V)$ manifests on the order of 10^3 in the molecular break junction upon reaching the atomic wire limit. If the electrode is reverted to a nanowire, still with only one gold atom contacting sulfur, the difference $(T_{\downarrow}-T_{\uparrow})(\varepsilon_f)$ has already diminished to zero. We reason that the reduced bond coordination of the interface gold atom with respect to the bulk electrode prompted a change in its covalent bonding with sulfur, disrupting the magnetic neutrality of primarily the sulfur $3p_z$, but also the gold 6s and $5d_{z^2}$ valence orbitals at the Au-S quantum-point interface.

Keywords: Density-functional theory (DFT), non-equilibrium Green's functions (NEGF), atomic wire (AW), quantum-point contact (QPC), Peierls distortion, gold-thiol, 1,4-benzenedithiol (1,4-BDT), spin valve

I. INTRODUCTION

At the quantum limit, the interface between a device and its ohmic contacts can dominate the electronic structure properties of the concatenated system. For all intents and purposes, this limit is represented by linear chains of individual atoms. Crystalline single atom chains of certain elements display perfect metallicity with a single quantum of conductance.[2] However, a metal-to-semiconducting transition occurs as phonons perturb the lattice, opening a forbidden energy gap. This phenomenon is known as the Peierls instability[3] and serves as an example of how adiabatic computational methods do not capture all of the physics, making essential time-dependence and electron-phonon (e-ph) terms in the Hamiltonian.[4–6] Experimental methods such as inelastic electron tunneling spectroscopy (IETS)[7–10] can elucidate the Peierls distortion and accompanying effects of e-ph interaction on the transport characteristics.

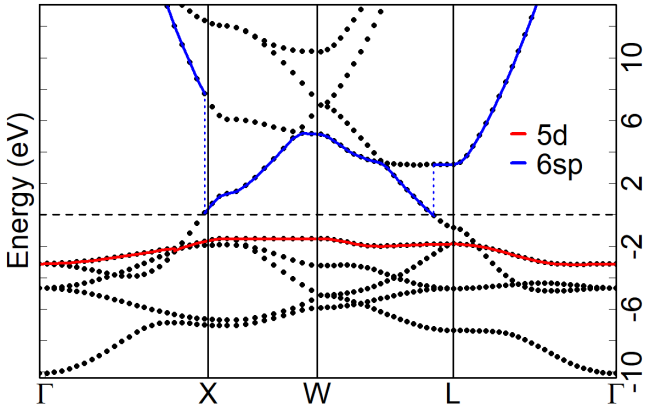

Figure 1: After Rangel et al[1]: Energy levels along the $\Gamma-X-W-L-\Gamma$ path in face-centered-cubic gold (FCC Au) Brillouin zone. The lattice parameter a = 4.08 Å. ε_f is the dotted line at 0 eV. Output from SIESTA using the Ceperley-Alder local density approximation (LDA).

Previous research has shown that inelastic scattering during transport through an Au atomic wire (AW) produces local heating, a conductance profile that drops slightly at bias, and the excitation of e-ph modes with strain at resonant values of bias.[11,12] Fabrication techniques involving mechanical break junctions or atomic force probes show that the Au AW are of highest stability at or below 7 atoms in length. Additionally, e-ph interactions in the short chains manifest a 3% decrease in conductance - which further decreases with bias and significantly decreases with the length of chain.[13]

The ballistic transport formalism employed in this work does not include e-ph scattering; the electronic mean-free-path is assumed to be much greater than the length of the lead-molecule-lead system. Thus, the non-diffusive assumption is more appropriate for shorter wire lengths, in order to provide qualitative data with regard to spin-dependent and resonant tunneling. Likewise, in the elastic regime, employing atomic chains of carbon as electrical leads, previous research has depicted the onset of resonant tunneling as narrow, isolated peaks in the zero bias transmission spectrum of a graphene nanoribbon heterojunction.[14]

Prior experiments, utilizing scanning tunneling microscopy (STM) under ultra-high vacuum (UHV) conditions, have investigated and imaged quantum point contacts (QPC).[15,16] Ab-initio calculations have revealed anisotropic magnetic moments on transition metal atomic wires and attributed these to the lessened coordination of the atoms closest to the center of the chain, noting sensitivity to parameters such as structure, temperature, and applied fields.[17] In a recent experiment, the onset of spin-polarized transport in atomic wires was predicted by observations of the lowest conduction peaks occurring at a value of 0.5 G_0.[18]

The 1,4-benzenedithiol (1,4-BDT) device[19–25] is a frequent object of study in the literature of nanoelectronics. Many possible applications for gold-thiol composite materials e.g. molecular break junctions, self-assembled monolayers (SAM), and thiolated Au nanoparticles (NP) have already been set forth. These range from molecular electronics and tunable plasmonics to mediated cell-uptake via shell-capping functionalization.[26–28] Occurences of magnetism at the Au-S interface have been explored and shown to have dependence on the bond coordination of the surface Au atoms with respect to the thiol end-group.[29,30] Presented in prior literature, theoretical spin filters have been found to operate according to the distribution of spin-orbitals with respect to energy.[31–33]

II. METHODOLOGY

A. SIESTA

Density-functional theory (DFT) is implemented in the Spanish Initiative for Electronic Simulations with Thousands of Atoms (SIESTA)[34] ab-initio package using Bloch wavefunctions with finite support in position and momentum space. Atomistic depiction of the unit cell is handled by the Visualization for Electronic and Structural Analysis (VESTA) program.[35] The localized pseudo-atomic orbital (PAO) basis set, generated within SIESTA, is denoted double-zeta with polarization (DZP).[36,37] Exchange-correlation terms are described by either the local density approximation (LDA) or the generalized gradient approximation (GGA).[38] Norm-conserving Troullier-Martins pseudopotentials, which are non-relativistic and lack core correction, were generated by ATOM, a Fortran code written by Sverre Froyen and maintained by Alberto Garcia.[39,40]

The conjugate gradients option in SIESTA relaxes the magnitude of force in three orthogonal directions at each atomic position to a maximum tolerance of 0.01 eV/Å. Output data from SIESTA for graphical depiction includes the energy-momentum (E-k) band structures, Mulliken populations, density of states (DOS), and projected density of states (PDOS). The lattice constant for FCC Au (4.08 Å) is consistent with literature and the $\Gamma - X - W - L - \Gamma$ band structure (Fig. 1) shows similarity with respect to the 5d and 6sp bands near ε_f.[1] ε_f, the Fermi energy, is found between the energies of the valence band maximum (VBM) and conduction band minimum (CBM) and may be set to zero by translating the band eigenvalues.

B. TranSIESTA

In order to simulate a system out of chemical equilibrium within the SIESTA framework, the crystalline unit cell becomes the region of scattering, partitioned into three subspaces (left electrode, device, right electrode). Rigid shifts of $-\frac{V_b}{2}$ and $+\frac{V_b}{2}$ are applied to the chemical potentials of the left and right electrodes, $\mu_{L,R}$, on either side of the central device region to simulate an applied bias voltage V_b (Eq. 1). k_BT is set to 25 meV in order to construct the Fermi-Dirac distribution for electronic states in the left and right leads, $f_{L,R}$ (Eq. 2). The non-equilibrium Green's function (NEGF) expansion, TranSIESTA and TBTrans[41,42] together produce the spin-resolved transmission coefficient T(E,V_b). The current-voltage characteristic I(V_b) is formed by plotting the current at each 10 mV step in V_b, using the Landauer integral (Eq. 3)[43] implemented in TBTrans. At $V_b = 0$, the energy discretization is at least 1 meV for the DOS and T(E), and 2 meV for these functions at non-zero V_b when retrieving the elastic current at bias.

$$\varepsilon_f = \mu_L - \frac{V_b}{2} = \mu_R + \frac{V_b}{2} \tag{1}$$

$$f_{L,R} = \frac{1}{e^{(E-\mu_{L,R})/k_BT} + 1} \tag{2}$$

$$I = \frac{2e}{h}\int_{-\infty}^{\infty} dE(f_L - f_R)T(E) \tag{3}$$

III. RESULTS

A. Peierls Distortion Test

The Cartesian atomic coordinates ascribed to the electrode and device subspaces must be expressed to precision within two distinct sets of boundary conditions: a fully-infinite superlattice vs. semi-infinite crystalline electrodes ohmically contacting a central device. The formalism sprouts atomic forces on the electrode and interface atoms which should resolve into crystal strain at the electrode-device interface by modifying the supercell (see Appendix). The Peierls instability criterion ($\vec{G} > 2\vec{k}_f$) suggests an additional phase transition due to the lead-molecule (LM) lattice mismatch plus the semi-infinite (LCR) boundary condition ($\vec{G}_{eff} = \vec{G}_{LM} + \vec{G}_{LCR}$). The maximum force on any one atom along the longitudinal axis of the atomic wire (due to ohmic contacts with 1,4-BDT) is found to be about 0.5 eV/Å.

As follows, the Peierls distortion is emulated within the Au AW to quantify the effect of atomic displacement on the transport properties of the 1-D lattice. The crystalline Au AW is implemented in SIESTA in a dimerized unit cell with interatomic spacing of 2.464 Å. The symmetrized unit cell becomes the left and right electrode to a central dimer which is perturbed by a displacement in Å, $\delta \in \{0.1, 0.2, 0.3\}$. The Peierls distortion stemming from δ is quantifiable in I(V) and T(E) (Fig. 2). Indicative of a charge density wave, T(E) and the differential conductance (dI/dV) are marginally diminished in the perturbed wires while the step-function profile denoting the G_0 eigenchannels is retained.[44]

In this contribution, the reported data and figures employ 290°K for the electronic temperature in the Fermi-Dirac distribution. The procedure outlined above (Fig. 2) is repeated at statistical fermionic occupation temperatures of 4.2 °K and 77 °K, to investigate the use of room temperature in Eq. 2.

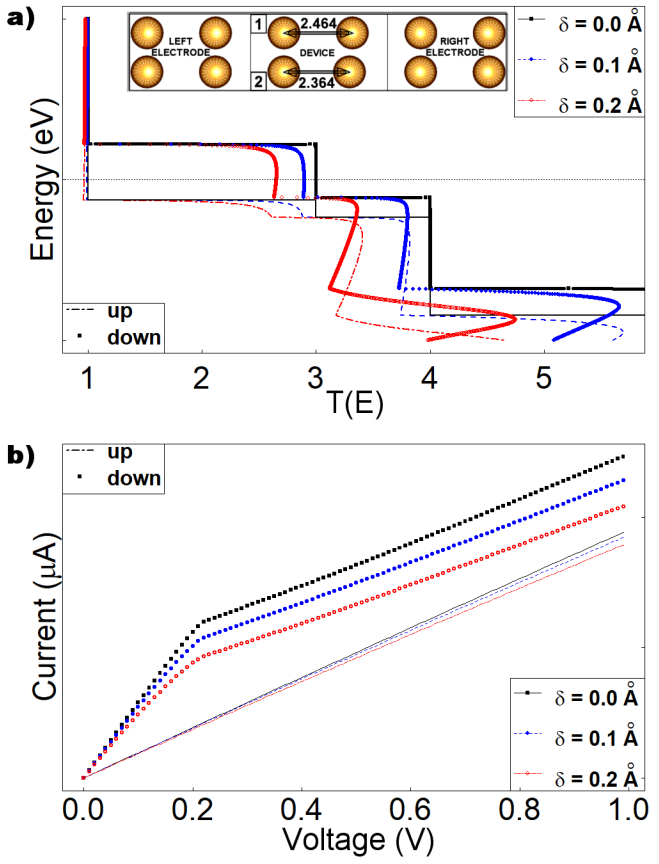

Figure 2: a) Spin-resolved T(E) at zero bias for three Au AWs each with a 1-D displacement of $\delta = 0.0$, 0.1, and 0.2 Å. ε_f is the dotted line at E = 0 eV. Inset: Unit cell visualization of the $\delta = 0.1$ Å displacement in 1-D Au. Bond lengths are given in Å for the unperturbed [1] and perturbed [2] atomic wires. b) Corresponding I(V) curves for the same three scattering regions.

The I(V_b) curves were compared to find a maximum percent deviation of only 0.2% between values of current.

B. Projected Density of States

For three Au-BDT superlattices, each with a distinct Au electrode arrangement, the DOS is projected onto the orbitals belonging to the Au-S interface (Fig. 3). The plot for the system with AW electrodes stands out uniquely at first glance with spin-occupation differentials present in the interface Au 6s and $5d_{z^2}$ orbitals as well as the S $3p_z$ orbital (Fig. 3(a)). On the other hand, the nanowire (NW) electrode system displays no significant magnetization (Fig. 3(b)). The self-assembled monolayer (SAM) system features the Au [001] plane bonding with sulfur via two atoms (Fig. 3(c)). Comparison of these three systems corroborates the use of the NW in a spin-independent setting.

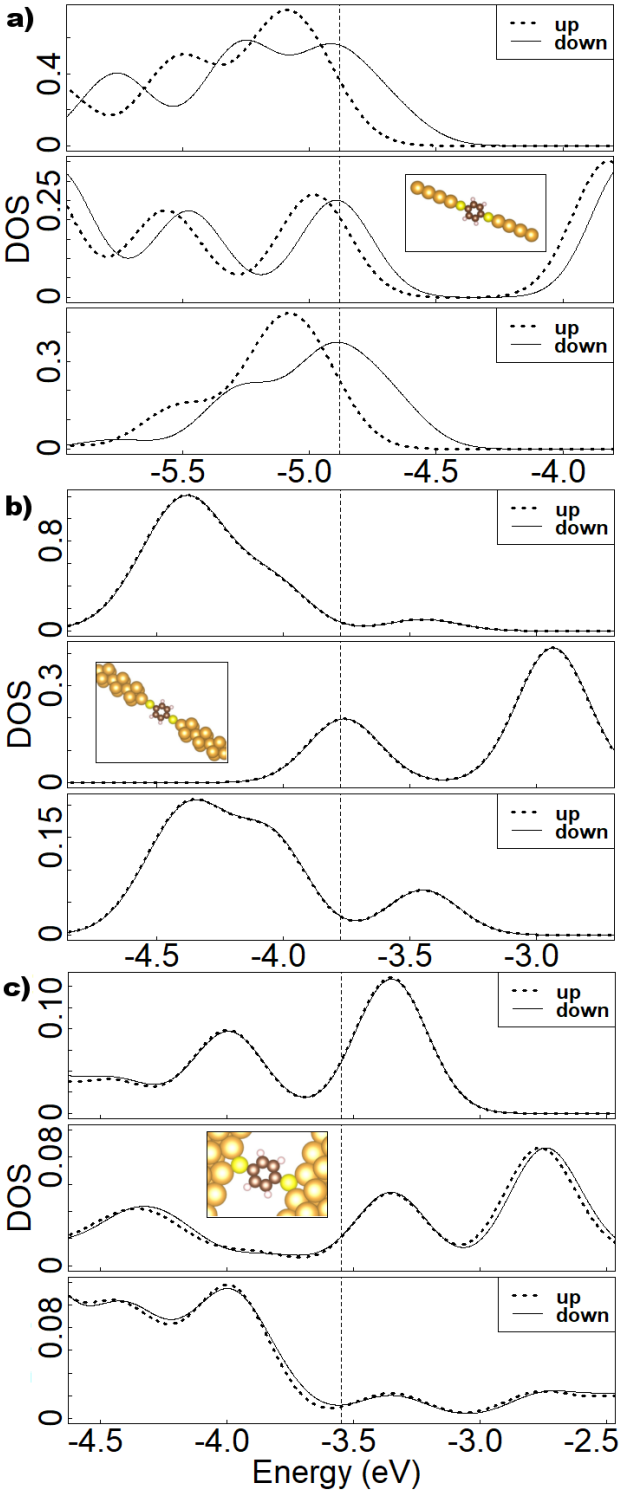

Figure 3: Spin-resolved PDOS for the S $3p_z$, Au 6s, and Au $5d_{z^2}$ orbitals (upper, middle, and lower, respectively) at the Au-S interface for 1,4-BDT attached to Au electrodes of type a) AW b) $\varnothing$ 0.4 nm NW c) [001] surface. Inset: 3-D visualizations of the scattering region unit cell with space-filling depiction of the atoms. ε_f is the dashed line at a) -4.88 eV b) -3.77 eV and c) -3.49 eV.

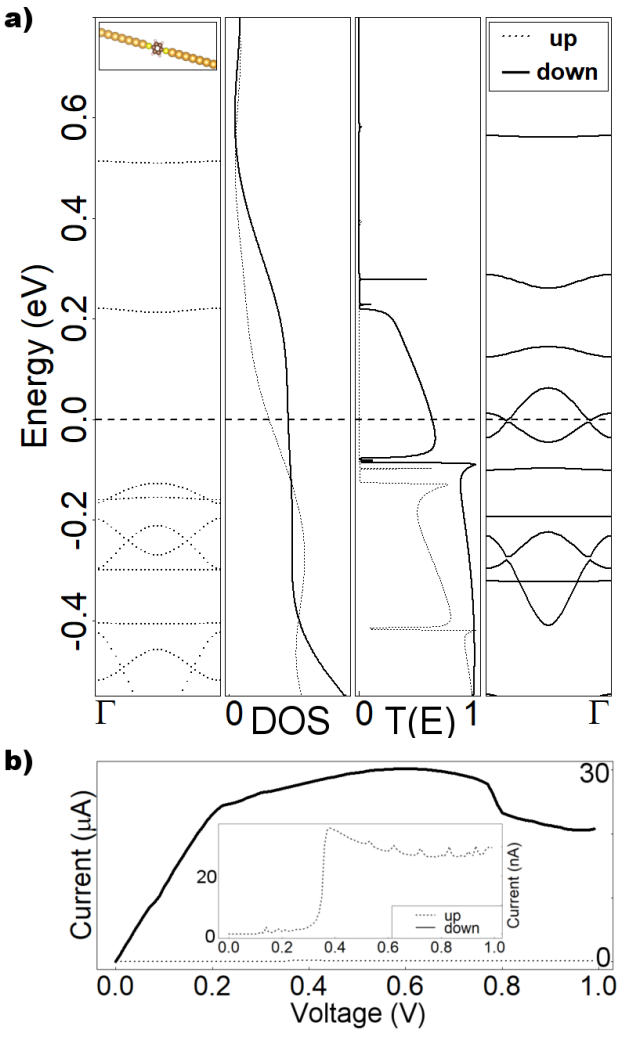

Figure 4: a) Depiction of the spin-polarized electronic structure for 1,4-BDT between Au AWs. From left to right: spin-↑ energy bands, spin-resolved total DOS, spin-resolved T(E) at zero bias, and spin-↓ energy bands. ε_f is the dashed line at E = 0 eV. Inset: Visualization of the region of scattering. b) Spin-resolved I(V) curve for 1,4-BDT between semi-infinite Au AWs. Inset: Magnification of $I_{\uparrow}(V)$.

C. Atomic Wires and 1,4-BDT

To reiterate, the Au-S interface PDOS for the AW system (Fig. 3(a)) relates available states for spin-↓ electrons - states exclusive to spin-↑ electrons - existing at energies at and just above ε_f. The Au 6s and $5d_{z^2}$, and the S $3p_z$ orbitals at the electrode-device interface remain closed to spin-↑ electrons in valence near ε_f. In other words, the one-dimensional ballistic scattering continuum is magnetized according to the preferred ground-state of these three orbitals at the lead-molecule interface (Au 6s, Au $5d_{z^2}$, and S $3p_z$).

The spin-resolved E(k), DOS, and T(E) diagrams are depicted for 1,4-BDT chemisorbed onto Au AW leads

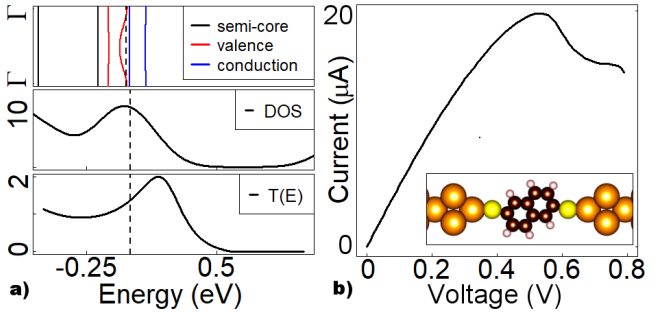

Figure 5: a) Spin-independent electronic structure for 2,6-NDT between ⌀ 0.4 nm NWs (from bottom to top: T(E,0), DOS, and energy bands). ε_f is the dashed line at E = 0 eV. b) Spin-independent I(V) curve for the system shown. Inset: Space-filling visualization. $I_{\uparrow}(V)$.

(Fig. 4(a)). A much more favorable probability of tunneling for the itinerant spin-↓ exists: $T_{\uparrow}(E_f) = 1.72 * 10^{-3}$ and $T_{\downarrow}(E_f) = 0.48$ (at zero-bias). In the I(V) curve (Fig. 4(b)), the spin filtration ratio $(I_{\downarrow}/I_{\uparrow})(V)$ manifests to three orders of magnitude (e.g. $1.61 * 10^3$ at $V_b = 25$ mV). The feature near 0.2 V is of interest, where the $(dI/dV)_{\downarrow}$ drops coincidentally with the opening of the lowest quasi-bound spin-↑ band. Distribution of single-particle spins according to the orbital angular momentum channels[45] (Hund's Rules), the solely linear (1-D) bonding coordination, and the Au-S QPC, are posited collectively to describe these features at low energy.

D. Spin-independent Characterization

The spin-independent ⌀ 0.4 nm NW electrode brings into question the presence of magnetic anisotropy within the device subspace. For instance, consider the chiral (armchair or zigzag) edge structure of a di-thiol functionalized aromatic molecule: the isomorph of 1,4-biphenyl-dithiol (1,4-BPDT) in the hexagonal-planar lattice, 2,6-naphthalene-dithiol (2,6-NDT), is spectralized by TranSIESTA near the Fermi energy (ε_f) within the gold-thiol molecular junction (Fig. 5). Depictions of the electronic structure reveal no evidence of ground-state spin-splitting in this junction, and the superlattice is predicted to exhibit metallic behavior near ε_f.

The device operates as expected for a negative differential resistance (NDR) device with a low peak-to-valley ratio (PVR) due to confinement of the LUMO state near the Fermi level. In varying the molecule, while keeping the ⌀ 0.4 nm NW electrodes, the device figures-of-merit for the gold-thiol junction improve as the number of conjugated phenyl rings is increased ∈{1,4-BDT,1,4-BPDT,1,4-TPDT} (Table I).

IV. CONCLUSION

Characterization of gold-thiol junctions is carried out independently of spin (given a non-magnetic molecule) when employing the ⌀ 0.4 nm NW. DFT-NEGF simulations of Au

Table I: Spin-independent figures-of-merit for the molecular devices attached to NW electrodes. $V_{H,L}$ are the operation voltages in V and ($I_{H,L}$) are the high and low currents reported in μA. The NDR ($\Delta V/\Delta I$) is given in $k\Omega$ between the H and L points, and I_H/I_R is the peak-to-valley ratio (PVR).

⌀ 0.4 nm NW						
Device	$\mathbf{V_H}$	$\mathbf{V_L}$	$\mathbf{I_H}$	$\mathbf{I_L}$	**PVR**	**NDR**
1,4-BDT	0.90	0.66	22.44	13.54	1.658	-38.20
1,4-BPDT	0.44	0.57	20.48	4.84	4.230	-8.125
1,4-TPDT	0.45	0.56	16.72	2.61	6.408	-7.795
2,6-NDT	0.54	0.80	19.78	8.34	2.370	-31.47

AWs attached to 1,4-BDT detect magnetotransport at low bias: a spin filtration ratio $(I_\downarrow/I_\uparrow)(V)$ on the order of 10^3. The ballistic I(V_b) of the bare AW electrode is observed to diminish only slightly in response to phonon-like mechanical perturbation. Experimental verification of the reported observations may take place within an IETS setup. As evidenced by the Peierls distortion, the actual electronic structure and transport characteristics of a 1-D superlattice depend upon the inelastic corrections as a function of time, voltage, and temperature.

References

[1] T. Rangel, D. Kecik, P. Trevisanutto, G.-M. Rignanese, H. Van Swygenhoven, and V. Olevano, Physical Review B **86**, 125125 (2012).

[2] C. Kittel, *Introduction to Solid State Physics*, 8th ed. (John Wiley & Sons, Inc., 2005) Chap. 18, pp. 528–538.

[3] R. E. Peierls, *Quantum Theory of Solids*, 23rd ed. (Oxford University Press, 1955).

[4] T. Frederiksen, M. Brandbyge, N. Lorente, and A.-P. Jauho, Physical Review Letters **93**, 256601 (2004).

[5] T. Frederiksen, M. Paulsson, M. Brandbyge, and A.-P. Jauho, Physical Review B **75**, 205413 (2007).

[6] A.-P. Jauho, N. S. Wingreen, and Y. Meir, Physical Review B **50**, 5528 (1994).

[7] M. Galperin, M. A. Ratner, and A. Nitzan, Journal of Physics: Condensed Matter **19**, 103201 (2007).

[8] A. Troisi and M. A. Ratner, Small **2**, 172 (2006).

[9] A. Troisi and M. A. Ratner, Nano Letters **6**, 1784 (2006).

[10] M. Taniguchi, M. Tsutsui, K. Yokota, and T. Kawai, Nanotechnology **20**, 434008 (2009).

[11] L. de La Vega, A. Martin-Rodero, N. Agraït, and A. L. Yeyati, Physical Review B **73**, 075428 (2006).

[12] N. Agraït, C. Untiedt, G. Rubio-Bollinger, and S. Vieira, Physical Review Letters **88**, 216803 (2002).

[13] N. Agraıt, A. L. Yeyati, and J. M. Van Ruitenbeek, Physics Reports **377**, 81 (2003).

[14] H. Sevinçli, M. Topsakal, and S. Ciraci, Physical Review B **78**, 245402 (2008).

[15] H. Ohnishi, Y. Kondo, and K. Takayanagi, Nature **395**, 780 (1998).

[16] D. M. Eigler and E. K. Schweizer, Nature **344**, 524 (1990).

[17] V. Stepanyuk, A. Klavsyuk, W. Hergert, A. Saletsky, P. Bruno, and I. Mertig, Physical Review B **70**, 195420 (2004).

[18] V. Rodrigues, J. Bettini, P. C. Silva, and D. Ugarte, Physical Review Letters **91**, 096801 (2003).

[19] P. Damle, A. W. Ghosh, and S. Datta, Chemical Physics **281**, 171 (2002).

[20] M. A. Reed, C. Zhou, C. Muller, T. Burgin, and J. Tour, Science **278**, 252 (1997).

[21] E. G. Emberly and G. Kirczenow, Chemical Physics **281**, 311 (2002).

[22] K. Stokbro, J. Taylor, M. Brandbyge, J.-L. Mozos, and P. Ordejon, Computational Materials Science **27**, 151 (2003).

[23] A. Nitzan and M. A. Ratner, Science **300**, 1384 (2003).

[24] M. Strange, C. Rostgaard, H. Häkkinen, and K. S. Thygesen, Physical Review B **83**, 115108 (2011).

[25] N. Sergueev, D. Roubtsov, and H. Guo, Physical Review Letters **95**, 146803 (2005).

[26] J. Chen, W. Wang, M. Reed, A. Rawlett, D. Price, and J. Tour, Applied Physics Letters **77**, 1224 (2000).

[27] M. D. Malinsky, K. L. Kelly, G. C. Schatz, and R. P. Van Duyne, Journal of the American Chemical Society **123**, 1471 (2001).

[28] D. A. Giljohann, D. S. Seferos, W. L. Daniel, M. D. Massich, P. C. Patel, and C. A. Mirkin, Angewandte Chemie International Edition **49**, 3280 (2010).

[29] A. Ayuela, P. Crespo, M. García, A. Hernando, and P. M. Echenique, New Journal of Physics **14**, 013064 (2012).

[30] J. De La Venta, E. Fernandez Pinel, M. Garcia, P. Crespo, A. Hernando, O. R. De La Fuente, C. De Julián Fernández, A. Fernández, and S. Penadés, Modern Physics Letters B **21**, 303 (2007).

[31] J. Zeng and K.-Q. Chen, Journal of Materials Chemistry C **1**, 4014 (2013).

[32] W. J. Cho, Y. Cho, S. K. Min, W. Y. Kim, and K. S. Kim, Journal of the American Chemical Society **133**, 9364 (2011).

[33] F. Zu, Z. Liu, K. Yao, G. Gao, H. Fu, S. Zhu, Y. Ni, and L. Peng, Scientific Reports **4**, 4838 (2014).

[34] J. M. Soler, E. Artacho, J. D. Gale, A. García, J. Junquera, P. Ordejón, and D. Sánchez-Portal, Journal of Physics: Condensed Matter **14**, 2745 (2002).

[35] K. Momma and F. Izumi, Journal of Applied Crystallography **44**, 1272 (2011).

[36] M. Strange, I. Kristensen, K. S. Thygesen, and K. W. Jacobsen, The Journal of Chemical Physics **128**, 114714 (2008).

[37] D. Sánchez-Portal, E. Artacho, and J. M. Soler, Journal of Physics: Condensed Matter **8**, 3859 (1996).

[38] J. P. Perdew, K. Burke, and M. Ernzerhof, Physical Review Letters **77**, 3865 (1996).

[39] N. Troullier and J. L. Martins, Physical Review B **43**, 1993 (1991).

[40] S. G. Louie, S. Froyen, and M. L. Cohen, Physical Review B **26**, 1738 (1982).

[41] M. Brandbyge, J.-L. Mozos, P. Ordejón, J. Taylor, and K. Stokbro, Physical Review B **65**, 165401 (2002).

[42] N. Papior, N. Lorente, T. Frederiksen, A. García, and M. Brandbyge, Computer Physics Communications **212**, 8 (2017).

[43] Y. Meir and N. S. Wingreen, Physical Review Letters **68**, 2512 (1992).

[44] R. E. Thorne, Physics Today.

[45] M. Koskinen, M. Manninen, and S. Reimann, Physical Review Letters **79**, 1389 (1997).